PHYSICAL REVIEW B VOLUME 47, NUMBER 7 15 FEBRUARY 1993-I

Electron mobilities in modulation-doped $Al_xGa_{1-x}As/GaAs$ and pseudomorphic $Al_xGa_{1-x}As/In_yGa_{1-y}As$ quantum-well structures

Kaoru Inoue and Toshinobu Matsuno
Semiconductor Research Center, Matsushita Electric Industrial Co. Ltd.,
3-15, Yagumo-Nakamachi, Moriguchi, Osaka 570, Japan
(Received 30 June 1992)

Electron mobilities in modulation-doped $Al_xGa_{1-x}As/GaAs/Al_xGa_{1-x}As$ and pseudomorphic $Al_xGa_{1-x}As/In_yGa_{1-y}As/Al_xGa_{1-x}As$ quantum-well structures with high electron concentration have been measured in order to clarify their dependences on the quantum-well thickness. It has been found that the 77-K mobilities show their highest values for quantum-well widths ranging from 80 to 100 Å. To understand the experimental results, mobility calculations were performed using a two-subband transport model. The experimental dependences of electron mobility on the quantum-well thickness were reproduced in the theoretical calculations and it has been found that the conditions for the highest mobilities at 77 K correspond to the case when the Fermi energies of electrons in the ground subband become maximum with almost all the electrons populating in the ground subband. For wider quantum-well thicknesses, electrons begin to populate in the upper subband, which results in sudden reduction in electron mobilities due to the sudden increase of intersubband scattering rate and reductions in Fermi energies of electrons in the ground subband.

I. INTRODUCTION

Mobilities of the two-dimensional electron gas in modulation-doped $Al_xGa_{1-x}As/GaAs$ heterostructures have been extensively researched both experimentally and theoretically in recent years. Although quantitative comparisons between theory and experiment were performed by many researchers, most of the previous works have been concerned with the case where electrons occupy only the ground subband.[1,2] In modulation-doped quantum-well structures with high electron concentrations, however, electrons can populate over several subbands even at low temperatures and mobilities are expected to be greatly affected by the quantum-well width (L_z) because subband energy levels or their spacings change drastically with L_z. From the viewpoint of device applications, it will be important to understand how low-field mobilities change with L_z for modulation-doped quantum-well structures. In order to calculate the mobility in such structures, a multisubband transport problem must be treated. Such a problem was previously treated by Mori and Ando[3] to analyze the low-temperature electron mobilities due to the interface roughness scattering and ionized impurity scattering in Si metal-oxide-semiconductor structures based on a theory developed by Sigga and Kwock.[4] For modulation-doped $Al_xGa_{1-x}As/GaAs$ heterostructures, although simplified calculations at 0 K and phonon-limited mobilities at 77 and 300 K have been reported so far,[5–7] the dependence of mobility on the quantum-well width has not been well studied yet.

In this paper, we have studied the electron mobilities in modulation-doped $Al_xGa_{1-x}As/GaAs$ and $Al_xGa_{1-x}As/In_yGa_{1-y}As$ quantum-well structures both experimentally and theoretically. For calculations, we have applied a two-subband model and solved coupled Boltzmann's equations using self-consistent wave functions and temperature-dependent screening parameters. For the polar optical scattering, we adopted the iteration method developed by Nag.[8] The calculated results were compared with the experimental data and the relative importance of scattering mechanisms has been clarified in these heterostructures.

II. OUTLINE OF MOBILITY CALCULATION

In this section, theoretical models and calculation methods adopted in this work are briefly described. The electronic state in the quantum well is characterized by the subband index i and a two-dimensional wave vector $\mathbf{k}=(k_x,k_y)$ parallel to the surface. The wave function and energy are, respectively, given by

$$\psi_{i,\mathbf{k}}(\mathbf{r},z)=\frac{1}{S^{1/2}}\zeta_i(z)\exp(i\mathbf{k}\cdot\mathbf{r}) \ , \tag{1}$$

$$E_{i,\mathbf{k}}=E_i+\frac{\hbar^2k^2}{2m^*} \ , \tag{2}$$

where $\zeta_i(z)$ denotes the quantized wave function, m^* the electron effective mass, and $\hbar$ the reduced Planck constant. The set of Boltzmann equations for the electron distribution function for subband i, $\phi^{(i)}(\mathbf{k})$, may be written as

$$-\frac{e\mathbf{F}}{\hbar}\nabla_{\mathbf{k}}f^{(i)}(\mathbf{k})=\sum_{j,\mathbf{k}'}\{P_{ji}(\mathbf{k}',\mathbf{k})f^{(j)}(\mathbf{k}')[1-f^{(i)}(\mathbf{k})] -P_{ij}(\mathbf{k},\mathbf{k}')f^{(i)}(\mathbf{k})[1-f^{(j)}(\mathbf{k}')]\} \ , \tag{3}$$

where $P_{ij}(\mathbf{k},\mathbf{k}')$ is the probability per unit time for an

 ©1993 The American Physical Society

electron in a state $\mathbf{k}$ of subband i to transfer to a state $\mathbf{k}'$ of subband j and $\mathbf{F}$ is the electric field applied parallel to the heterointerface. For a vanishingly small electric field, we may expand the distribution function $f^{(i)}(\mathbf{k})$ for each subband as

$$f^{(i)}(\mathbf{k})=f_0(E_{i,\mathbf{k}})+\frac{e\hbar}{m^*}\mathbf{F}\cdot\mathbf{k}\phi^{(i)}(\mathbf{k})\frac{\partial f_0(E_{i,\mathbf{k}})}{\partial E_{i,\mathbf{k}}} , \quad (4)$$

where $f_0(E_{i,\mathbf{k}})$ is the equilibrium Fermi-Dirac distribution function and $f^{(i)}(\mathbf{k})$ is the perturbation function to be determined from the Boltzmann equation. The principle of detailed balance is described as

$$P_{ij}(\mathbf{k},\mathbf{k}')f_0(E_{i,\mathbf{k}})[1-f_0(E_{j,\mathbf{k}'})] = P_{ji}(\mathbf{k}',\mathbf{k})f_0(E_{j,\mathbf{k}'})[1-f_0(E_{i,\mathbf{k}})] . \quad (5)$$

By using Eqs. (4) and (5) in Eq. (3) and neglecting the terms containing $\mathbf{F}$ of order higher than the second, Eq. (3) is simplified to the following form:

$$-\frac{e\mathbf{F}}{\hbar}\nabla_{\mathbf{k}}f_0(\mathbf{k})=\sum_{j,\mathbf{k}'}P_{ij}(\mathbf{k},\mathbf{k}')f_0(E_{i,\mathbf{k}})[1-f_0(E_{j,\mathbf{k}'})] \times\left[\frac{e\hbar}{m^*k_BT} \times\mathbf{F}\cdot\{\mathbf{k}\phi^{(i)}(\mathbf{k})-\mathbf{k}'\phi^{(j)}(\mathbf{k}')\}\right] . \quad (6)$$

Equation (6) is further simplified to the following equivalent equation:

$$1=\sum_{j,\mathbf{k}'}P_{ij}(\mathbf{k},\mathbf{k}')\frac{1-f_0(E_{j,\mathbf{k}'})}{1-f_0(E_{i,\mathbf{k}})}\left\{\phi^{(i)}(\mathbf{k})-\phi^{(j)}(\mathbf{k}')\frac{k'}{k}\cos\theta\right\} , \quad (7)$$

where θ is the angle between $\mathbf{k}$ and $\mathbf{k}'$. If we consider an elastic-scattering process and neglect the intersubband scattering, we obtain the following familiar equation:

$$\frac{1}{\phi^{(i)}(E)}=\sum_{\mathbf{k}'}P_{ii}(\mathbf{k},\mathbf{k}')(1-\cos\theta) . \quad (8)$$

The scattering mechanisms considered in this work are ionized impurity, acoustic phonon, alloy disorder, interface roughness, and polar optical-phonon scattering. The polar optical-phonon scattering was treated as an inelastic-scattering process and the screening effect for this scattering mechanism was neglected. Other scattering mechanisms were treated as elastic processes as usual and the screening effect was taken into account using the following equation:[9]

$$\tilde{V}_{ij}(q)=V_{ij}(q)+(e^2/2\varepsilon_0\kappa_0 q)\sum_{m,n}H_{ijmn}(q)\Pi_{mn}(q)\tilde{V}_{mn}(q) , \quad (9)$$

where $q=|\mathbf{k}-\mathbf{k}'|$, e is the elementary charge, ε_0 the dielectric permittivity, κ_0 the static dielectric constant, $V_{ij}(q)$ the unscreened matrix element, and $\tilde{V}_{ij}(q)$ is the screened one. The form factor $H_{ijmn}(q)$ and the polarization part $\Pi_{ij}(q)$ are given as follows:[10]

$$H_{ijmn}(q)=\int\int\zeta_i(z_1)\zeta_j(z_1)\zeta_m(z_2)\zeta_n(z_2) \times\exp(-q|z_1-z_2|)dz_1dz_2 , \quad (10)$$

$$\Pi_{ij}(q)=\sum_{\mathbf{k}'}\frac{f_0(E_{j,\mathbf{k}'})-f_0(E_{i,\mathbf{k}})}{E_{i,\mathbf{k}}-E_{j,\mathbf{k}'}} . \quad (11)$$

At zero temperature, $\Pi_{ij}(q)$ is calculated to be

$$\Pi_{ij}(q,0,E_F) = \frac{m^*}{\pi\hbar^2}\left[1-\frac{C_+}{2}\left\{\left[\frac{E_{ij}}{E_q}+1\right]^2-\left[\frac{2k_{F_i}}{q}\right]^2\right\}^{1/2} +\frac{C_-}{2}\left\{\left[\frac{E_{ij}}{E_q}-1\right]^2-\left[\frac{2k_{F_i}}{q}\right]^2\right\}^{1/2}\right] , \quad (12)$$

where $E_{ij}=E_i-E_j$, $E_q=\hbar^2q^2/2m^*$, $C_\pm=\mathrm{sgn}(E_{ij}\pm E_q)$, k_{F_i} is the Fermi wave number for subband i, and E_F is the Fermi energy. The temperature dependence of $\Pi_{ij}(q)$ is given as[11]

$$\Pi_{ij}(q,T,E_F)=\int_0^\infty\frac{\Pi_{ij}(q,0,E)}{4k_BT\cosh^2[(E_F-E)/2k_BT]}dE . \quad (13)$$

The unscreened scattering matrix element due to the ionized impurity (II) located at z_i is given by

$$V_{ij}^{\mathrm{II}}(q,z_i)=\frac{e^2}{2\varepsilon_0\kappa_0 q}\int\zeta_i(z)\zeta_j(z)\exp(-q|z-z_i|)dz , \quad (14)$$

and the scattering probability will be given by the sum of contributions from the whole region as

$$P_{ij}^{\mathrm{II}}(q)=\frac{2\pi}{\hbar}\int dz_iN(z_i)|\tilde{V}_{ij}^{\mathrm{II}}(q,z_i)|^2\delta(E_{i,\mathbf{k}}-E_{j,\mathbf{k}'}) , \quad (15)$$

where $N(z_i)$ is a concentration of ionized impurity located at z_i.

Scattering by acoustic phonons has two coupling modes; one is deformation-potential (DP) coupling and the other is piezoelectric (PE) coupling. The unscreened matrix elements due to these scattering mechanisms are, respectively, given by[1]

$$V_{ij}^{\mathrm{DP}}(q,q_z)=\left[\frac{D^2k_BT}{C_L}\right]^{1/2}I_{ij}(q_z) , \quad (16)$$

$$V_{ij}^{\mathrm{PE}}(q,q_z)=\left[\frac{e^2k_BTP^2}{2\varepsilon_0\kappa_0(q^2+q_z^2)}\right]^{1/2}I_{ij}(q_z) , \quad (17)$$

where D is the deformation-potential constant, C_L the longitudinal elastic constant, P the piezoelectric constant, and $I_{ij}(q_z)$ is defined by

$$I_{ij}(q_z)=\int\zeta_i(z)\zeta_j(z)\exp(-iq_zz)dz . \quad (18)$$

For the alloy scattering in $A_xB_{1-x}C$ type mixed crystals,

the following unscreened matrix element given by Harrison and Hauser[12] was employed:

$$V_{ij}^{\mathrm{AL}}(q,q_z)=[3\pi^2a^3x(1-x)(\Delta E)^2/64]^{1/2}I_{ij}(q_z)\ , \quad (19)$$

where ΔE is the alloy potential and a is the lattice constant. The alloy potential of 1 eV was used for the $Al_xGa_{1-x}As$ barrier layer and that for $In_yGa_{1-y}As$ was calculated using the Philips's electronegativity theory.[13] The transition probabilities due to acoustic phonons and alloy potentials are, respectively, given by the same formula as

$$P_{ij}(q)=\frac{2\pi}{\hbar}\int|\tilde{V}_{ij}(q,q_z)|^2\delta(E_{i,\mathbf{k}}-E_{j,\mathbf{k}'})dq_z\ . \quad (20)$$

As for the interface-roughness (IR) scattering, it was assumed that the roughness exists only at the bottom interface (substrate side at $z=z_B$) and the following matrix element given by Prange and Nee[14] was used:

$$V_{ij}^{\mathrm{IR}}(q)=\frac{\hbar^2}{2m^*}\left[\frac{d\zeta_i(z)}{dz}\frac{d\zeta_j(z)}{dz}\right]_{z=z_B}\times[\pi\Delta^2\Lambda^2\exp(-q^2\Lambda^2/4)]^{1/2}\ . \quad (21)$$

In the above equation, Δ and Λ are rms height and autocorrelation length for the roughness, respectively. The transition probability for this scattering is written as

$$P_{ij}^{\mathrm{IR}}(q)=\frac{2\pi}{\hbar}|V_{ij}^{\mathrm{IR}}(q)|^2\delta(E_{i,\mathbf{k}}-E_{j,\mathbf{k}'})\ . \quad (22)$$

For the elastic-scattering mechanisms described above, the perturbation function determined by each scattering mechanism $\phi^{(i)}(E)$ can be calculated as usual by introducing a symmetric matrix K whose elements are defined by

$$K_{ij}(E)=\sum_{\mathbf{k}'}\left[\delta_{ij}\sum_l P_{il}(\mathbf{k},\mathbf{k}')-P_{ij}(\mathbf{k},\mathbf{k}')\frac{k'}{k}\cos\theta\right]\ . \quad (23)$$

The perturbation functions are then expressed as

$$\phi^{(i)}(E)=\sum_j K_{ij}^{-1}(E)\ . \quad (24)$$

The mobility of the ith subband μ_i is given by

$$\mu_i=(e/m^*)\langle\phi^{(i)}(E)\rangle\ , \quad (25)$$

$$\langle\phi^{(i)}(E)\rangle=\int\phi^{(i)}(E)E\frac{\partial f_0(E)}{\partial E}dE\left[\int E\frac{\partial f_0(E)}{dE}dE\right]^{-1}\ . \quad (26)$$

Although the averaged mobility is often given by[10]

$$\bar{\mu}=\sum_i N_i\mu_i/N_s\ , \quad (27a)$$

where N_i is the electron concentration in the ith subband and N_s the total sheet electron concentration, the measured mobilities are Hall mobilities and the following equation, which was used in this paper, is considered to be more suitable for comparing the experimental results with calculations:[15]

$$\bar{\mu}=\sum_i N_i\mu_i^2\left[\sum_i N_i\mu_i\right]^{-1}\ . \quad (27b)$$

The polar optical-phonon scattering is an inelastic process accompanied by the absorption and emission of phonons with relatively large energy and is the dominant scattering process even at temperatures as low as 77 K. Although accurate estimations of mobilities due to this scattering mechanism require the solutions of a set of Boltzmann equations for several subbands, the actual calculation becomes more and more complex with the increase in the number of subbands under consideration. In this work, we have taken only two subbands into consideration for simplicity. In spite of this simplification, it is expected that the calculations will give good mobility estimations for the heterostructures with narrow quantum wells in which energy separations between subbands are relatively large.

First, let us consider the scattering processes which determine the perturbation function $\phi^{(0)}(E)$ for electrons in the ground subband. Figure 1 shows a schematic drawing of such processes, in which solid arrows indicate out-scattering processes and dashed arrows indicate in-scattering ones. A similar diagram can be drawn for electrons in the first exited subband. Using Eq. (7), the following equations can be obtained with regard to the perturbation functions, $\phi^{(0)}(E)$ and $\phi^{(1)}(E)$:

$$1=A_0(E)\phi^{(0)}(E)-B_0(E)\phi^{(0)}(E+\hbar\omega_{\mathrm{LO}})-C_0(E)\phi^{(0)}(E-\hbar\omega_{\mathrm{LO}})-D_0(E)\phi^{(1)}(E)-E_0(E)\phi^{(1)}(E+\hbar\omega_{\mathrm{LO}})-F_0(E)\phi^{(1)}(E-\hbar\omega_{\mathrm{LO}})\ , \quad (28a)$$

$$1=A_1(E)\phi^{(1)}(E)-B_1(E)\phi^{(1)}(E+\hbar\omega_{\mathrm{LO}})-C_1(E)\phi^{(1)}(E-\hbar\omega_{\mathrm{LO}})-D_1(E)\phi^{(0)}(E)-E_1(E)\phi^{(0)}(E+\hbar\omega_{\mathrm{LO}})-F_1(E)\phi^{(0)}(E-\hbar\omega_{\mathrm{LO}})\ . \quad (28b)$$

In coefficients $A_i(E)$, all the contributions from the out-scattering processes and intrasubband in-scattering processes are included. For example, in $A_0(E)$, the scattering processes numbered from 1 to 7 in Fig. 1 are included. Other coefficients are related with the in-scattering processes which are labeled as B, C, D, E, and F in Fig. 1. The out-scattering term due to polar optical-phonon scattering, $A_i^{\mathrm{PO}}(E)$, is written as

$$A_i^{\mathrm{PO}}(E)=\frac{m^*e^2\hbar\omega_{\mathrm{LO}}}{8\pi^2\varepsilon_0\hbar^3}\left[\frac{1}{\kappa_\infty}-\frac{1}{\kappa_0}\right]\frac{1}{1-f_0(E)}\sum_{j,\pm}[1-f_0(E\pm\hbar\omega_{\mathrm{LO}})](N_q+\tfrac{1}{2}\mp\tfrac{1}{2})\int\frac{|I_{ij}(q_z)|^2}{q_\pm^2+q_z^2}dq_z\ , \quad (29)$$

where N_q is an occupation number of the phonons. The forms for other in-scattering terms concerning polar optical scattering are easily obtained with small modifications by referring to the second term of the right-hand side in Eq. (7).

Equations (28a) and (28b) were solved by the iteration method proposed by Nag.[8] The starting values of $\phi^{(0)}(E)$ and $\phi^{(1)}(E)$ are obtained by taking only the first terms of the right-hand side in these equations. Thus,

$$\phi_0^{(0)}(E+n\hbar\omega_{\mathrm{LO}})=A_0(E+n\hbar\omega_{\mathrm{LO}})^{-1}\ , \tag{30a}$$

$$\phi_0^{(1)}(E+n\hbar\omega_{\mathrm{LO}})=A_1(E+n\hbar\omega_{\mathrm{LO}})^{-1}\quad (n=0,1,2,\ldots)\ . \tag{30b}$$

In the $(m+1)$th step of iteration, they were determined from

$$\begin{aligned}\phi_{m+1}^{(0)}(E+n\hbar\omega_{\mathrm{LO}})=A_0(E+n\hbar\omega_{\mathrm{LO}})^{-1}\{1&+B_0(E+n\hbar\omega_{\mathrm{LO}})\phi_m^{(0)}[E+(n+1)\hbar\omega_{\mathrm{LO}}]\\&+C_0(E+n\hbar\omega_{\mathrm{LO}})\phi_m^{(0)}[E+(n-1)\hbar\omega_{\mathrm{LO}}]+\cdots\\&+F_0(E+n\hbar\omega_{\mathrm{LO}})\phi_m^{(1)}[E+(n-1)\hbar\omega_{\mathrm{LO}}]\}\ ,\end{aligned} \tag{31a}$$

$$\begin{aligned}\phi_{m+1}^{(1)}(E+n\hbar\omega_{\mathrm{LO}})=A_1(E+n\hbar\omega_{\mathrm{LO}})^{-1}\{1&+B_1(E+n\hbar\omega_{\mathrm{LO}})\phi_m^{(1)}[E+(n+1)\hbar\omega_{\mathrm{LO}}]\\&+C_1(E+n\hbar\omega_{\mathrm{LO}})\phi_m^{(1)}[E+(n-1)\hbar\omega_{\mathrm{LO}}]+\cdots\\&+F_1(E+n\hbar\omega_{\mathrm{LO}})\phi_m^{(0)}[E+(n-1)\hbar\omega_{\mathrm{LO}}]\}\ .\end{aligned} \tag{31b}$$

Various material parameters used in the calculations are listed in Table I. The self-consistent wave functions, $\zeta_i(z)$ and each subband energy, E_i, necessary for the mobility calculations were calculated by solving the Schrödinger equation and the Poisson equation simultaneously.[16,17]

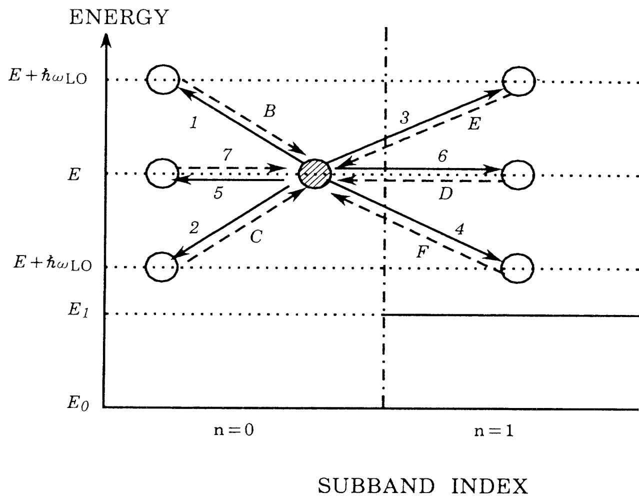

FIG. 1. Schematic diagram of scattering processes that contribute to $\phi_0(E)$. Shaded circle represents a state **k** of ground subband under consideration and open circles represent possible states **k**′ of either the ground or the first excited subband to which an electron is transferred from the shaded state **k** or vice versa. Two open circles on an equienergy plane with an energy E are concerned with elastic-scattering processes and four other open circles are concerned with polar optical-phonon scatterings that associate with phonon emissions or absorptions. Solid and dashed arrows indicate out-scattering and in-scattering processes, respectively. E_0 and E_1 are the lowest energies in the ground and first excited subband, respectively.

III. RESULTS AND DISCUSSIONS

All the samples used in this work were grown by molecular-beam epitaxy on (001) GaAs substrates at a substrate temperature about 530 °C. Two kinds of experiment were performed and the results were compared with the calculations. The first experiment was on the mobility dependence on the quantum-well width in modulation-doped $Al_xGa_{1-x}As/GaAs/Al_xGa_{1-x}As$ heterostructures and a similar experiment was performed using a pseudomorphic $In_yGa_{1-y}As$ quantum well as the second experiment. The sample structure for the first experiment is shown in Fig. 2. The AlAs mole fraction (x) in $Al_xGa_{1-x}As$ layers was 0.27 and the Si doping level (N_d) in n-type $Al_xGa_{1-x}As$ layers was $2\times10^{18}/\mathrm{cm}$.[3] The width of the GaAs quantum well was varied from 50 to 250 Å and sheet electron concentrations and mobilities were measured by Van der Pauw's method at 77 and 300 K. Square samples of typically 6 mm×6 mm were used for the mobility measurements. Ohmic contacts were formed by using InSn (90% In, 10% Sn) solder and annealing at 350 °C for 1 min. Care was taken for the size

TABLE I. Values of $In_xGa_{1-x}As$ material constants used in the mobility calculation.

Electron effective mass	$m^*=(0.067-0.044x)m_0$
Static dielectric constant	$\kappa_0=13.1+1.44x$
Optical dielectric constant	$\kappa_\infty=10.9+0.83x$
Deformation-potential constant	$D=8.6-2.8x$ (eV)
Piezoelectric constant	$P=0.052-0.0079x$
Longitudinal elastic constant	$C_L=13.97-3.99x$
LO-phonon energy	$\hbar\omega_{\mathrm{LO}}=36.11-0.707x$ (meV)
Lattice constant	$a=5.65325+0.40515x$ (Å)
Height (Δ) and	Δ=2.83 (Å)
lateral spread (Λ)	Λ=100 (Å)
of roughness	

Si-doped GaAs	100Å
Si-doped $Al_xGa_{1-x}As$	500Å
undoped $Al_xGa_{1-x}As$	20Å
undoped GaAs QW	(L_z)
undoped $Al_xGa_{1-x}As$	50Å
Si-doped $Al_xGa_{1-x}As$	150Å
undoped $Al_xGa_{1-x}As$	2000Å
undoped GaAs	1000Å
semi-insulating GaAs substrate	

($x=0.27, N_d=2x10^{18}/cm^3$)

FIG. 2. Cross-sectional diagram of the modulation-doped $Al_xGa_{1-x}As/GaAs/Al_xGa_{1-x}As$ heterostructure ($x=0.27$) used in the experiment.

and shape of Ohmic contacts so as to keep the errors in Hall voltage measurement less than 10% by referring to Ref. 18. The reproducibility of the Hall measurements was good; the variation of the measured results was within 5% for the two Van der Pauw chips from the same epitaxially grown wafer.

Calculated sheet electron concentrations and Fermi energies for each subband at 77 K as a function of quantum-well width are shown in Fig. 3 together with the measured N_s values. The agreement between experimental and calculated N_s values was found to be excellent when the value of conduction-band discontinuity (ΔE_c) of 270 meV was used. This value of ΔE_c is somewhat larger than the value of 200 meV that was determined by what is called Miller's rule[19] of $\Delta E_c/\Delta E_g=0.57-0.60$, where ΔE_g is the difference of energy gap between the two materials. In Fig. 3, it is seen that almost all the electrons populate in the lowest subband for the quantum-well width less than 100 Å at 77 K. For the quantum-well width from 100 to 200 Å, electrons populate in both the ground and first exited subbands and a negligibly small fraction of them in the second exited subband. Thus, the two subband transport model will be at least valid for quantum-well width less than 200 Å and at low temperatures below 77 K. In this paper, we have adopted this model also for higher-temperature regions as an approximation.

The calculated and experimental results on the mobility variations at 77 K as a function of quantum-well width are shown in Fig. 4. The agreement between them is seen to be good. As expected from the Fig. 3, a clear drop in electron mobility was observed in the region of quantum-well width from 100 to 150 Å. This is due to the fact that with the increase of quantum-well width, a transition from single-subband transport to two-subband transport occurs at a quantum-well width of about 100 Å and intersubband scattering probabilities increase drastically around this quantum-well width. From the figure, it is seen that the most dominant scattering process in these heterostructures is ionized impurities and that polar optical phonons are of second importance. Since the mobility limited by polar optical-phonon scattering is almost constant for a wide range of quantum-well width, the dependence of total mobility on the quantum-well width is largely determined by the change of the ionized impurity limited mobility. It should be noted here that the mobility peak due to the onset of a two-subband transport appears at a relatively narrow quantum-well width for

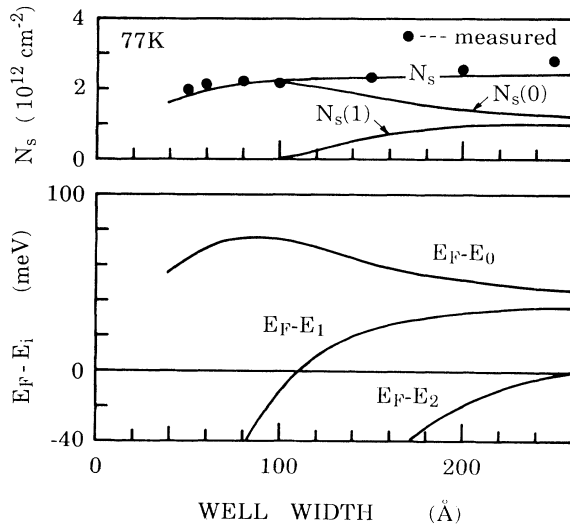

FIG. 3. Calculated sheet electron concentration and Fermi energy for each subband in $Al_xGa_{1-x}As/GaAs/Al_xGa_{1-x}As$ heterostructures ($x=0.27$) at 77 K as a function of GaAs quantum-well width. Measured values of sheet electron concentration are plotted by solid circles.

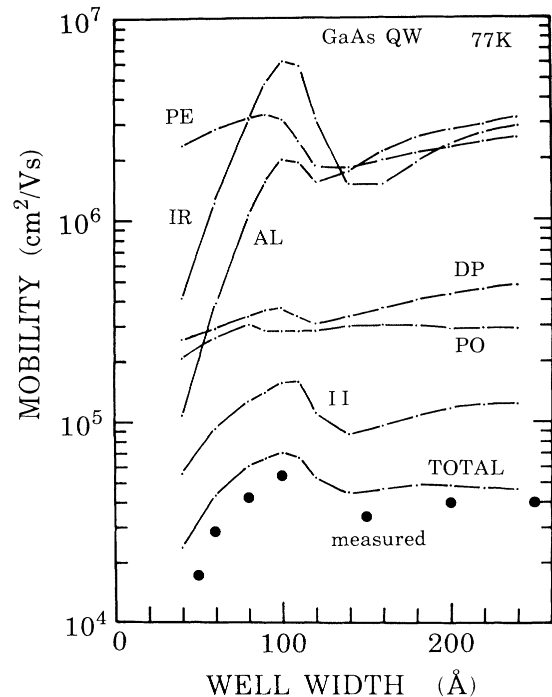

FIG. 4. Calculated and measured electron mobility in $Al_xGa_{1-x}As/GaAs/Al_xGa_{1-x}As$ heterostructures ($x=0.27$) at 77 K as a function of GaAs quantum-well width.

polar optical-phonon scattering limited mobilities. This is because the energy of the polar optical phonon is large (about 36 meV) and consequently the intersubband scattering can easily occur when the separation of the Fermi level and the level of the first exited subband energy is large but smaller than the phonon energy.

The alloy scattering is caused by the penetration of wave functions into the $Al_xGa_{1-x}As$ barrier layers. Thus, the mobility determined by this scattering mechanism becomes lower with the decrease of quantum-well width.

In the calculation of interface roughness limited mobility, we assumed the height of roughness is one monolayer (2.83 Å) and the lateral size was chosen to be 100 Å, a value near the minimum mobility in this scattering contribution. It is well known that the interface roughness limited mobility increases in proportion to the power of 6 of quantum-well width according to a simple calculation for a single-subband transport in a quantum well with infinitely high barriers.[20,21] For a quantum-well width smaller than 100 Å in the present case, the calculated mobility increases rapidly with the increase of the well width as expected from such a previous theory. When the two-subband transport initiates, however, a severe decrease in the calculated mobility is seen to occur. This is explained as follows. In the present case, it is assumed that the roughness exists only at the bottom heterointerface as described in the previous section and the potential of the quantum well is slightly asymmetric. This asymmetry makes electrons in the first excited subband more likely to accumulate near the bottom heterointerface where the interface roughness exists. Therefore, the electron mobility in the first excited subband limited by the interface roughness will show quite low values at the onset of the two-subband transport when the quantum-well width is not so large. The electron mobility in the ground subband is also deteriorated by the low mobility in the first excited subband through intersubband scattering. For example, when the quantum-well thickness was 120 Å, the calculated electron mobility for the first excited subband was 4.6×10^4 $cm^2/V\,s$, while that for the ground subband was $3.3\times10^6 cm^2/V\,s$. Since this scattering mechanism is not dominant in the present heterostructures, no clear evidence supporting the above calculated results has been obtained in the experimental results.

All the calculated mobilities are seen to be higher than the experimental ones by about 30% or more. These discrepancies are considered to be caused mainly by the fact that the doping profile of Si in n-type $Al_xGa_{1-x}As$ is not ideal due to the surface migration effects of dopants during the molecular-beam-epitaxy growth.[22] If such an effect is included properly, the agreement between the calculated and experimental results will be improved.

Figure 5 shows the calculated and experimental results on the mobility variations at 300 K as a function of quantum-well width. At this temperature, quantum-size effects are almost blurred out and no clear-cut reduction in mobility is seen. The mobilities are almost determined by the polar optical-phonon scattering and the calculated mobilities are almost constant for all the quantum-well width. For the quantum-well width about 100 Å, the agreement between the calculation and the experiment is better than that at 77 K. The differences between them, however, tend to become larger in the regions of quantum-well width smaller than 80 Å and larger than 150 Å. The cause for the differences in the wider well-width region is probably due to limitation of the two-subband transport model itself as described previously. For the differences in the narrower well-width region, however, it is not clear but a parallel conduction in n-type $Al_xGa_{1-x}As$ layers may affect the measured mobility values of the two-dimensional electron gas at 300 K.

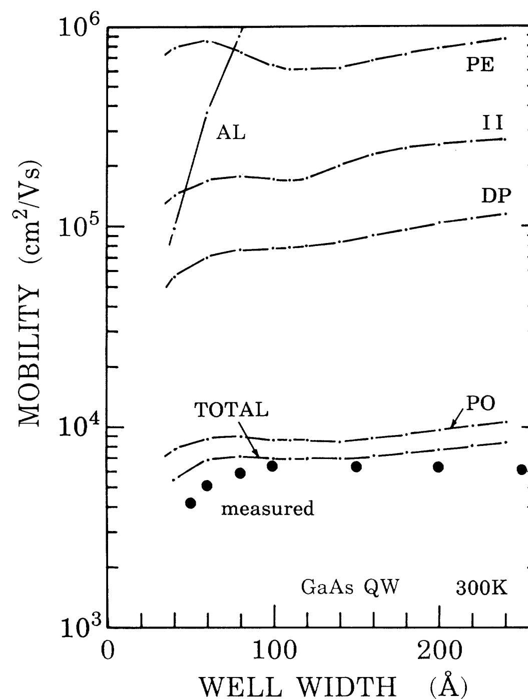

FIG. 5. Calculated and measured electron mobility in $Al_xGa_{1-x}As/GaAs/Al_xGa_{1-x}As$ heterostructures ($x=0.27$) at 300 K as a function of GaAs quantum-well width.

Next, similar experiments and calculations were performed for the modulation-doped pseudomorphic $Al_xGa_{1-x}As/In_yGa_{1-y}As/Al_xGa_{1-x}As$ quantum-well heterostructures. The sample structure is the same as that shown in Fig. 2 except that the GaAs quantum well was replaced by an $In_yGa_{1-y}As$ pseudomorphic layer with an InAs mole fraction (y) of 15%. The calculated sheet electron concentration and Fermi energy for each subband at 77 K are shown in Fig. 6 as a function of quantum-well width. The conduction-band discontinuity was calculated including the strain effect[23] and we have used the $\Delta E_c/\Delta E_g$ value of 0.8 in order to fit the calculated electron concentrations to the measured ones. Thus, the ΔE_c value of 395 meV was used. In these heterostructures at 77 K, the two-subband transport must be taken into consideration for the quantum-well width wider than 80 Å and the three-subband transport for 180 Å for the mobility calculations.

Figure 7 shows the calculated and measured electron mobilities for the modulation-doped $Al_xGa_{1-x}As/$

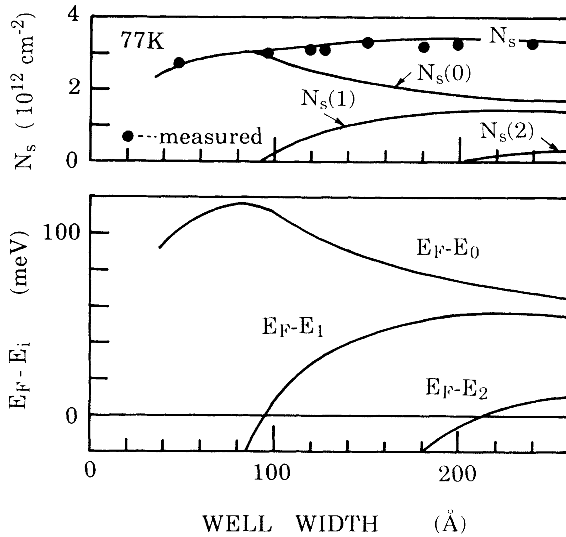

FIG. 6. Calculated sheet electron concentrations and Fermi energy for each subband in $Al_xGa_{1-x}As$/$In_yGa_{1-y}As$/$Al_xGa_{1-x}As$ heterostructures ($x=0.27$, $y=0.15$) at 77 K as a function of $In_yGa_{1-y}As$ quantum-well width. Measured values of sheet electron concentration are plotted by solid circles.

$In_yGa_{1-y}As$/$Al_xGa_{1-x}As$ pseudomorphic quantum-well structures at 77 K. The mobilities limited by ionized impurity scattering are higher than those in $Al_xGa_{1-x}As$/GaAs/$Al_xGa_{1-x}As$ structures by a factor of about 2 due to the lighter effective electron mass and larger Fermi energies. The most dominant scattering mechanism in this case is the alloy disorder, the mobilities limited by which show the same dependences on the quantum-well width as those limited by the acoustic deformation-potential scattering. As a result, the mobility drop at the onset of the two-subband transport is seen to be rather small. Nevertheless we can observe a clear dip in the experimental data in Fig. 7. The overall agreement between experimental and calculated mobilities is excellent. The differences between them, however, tend to become larger for the quantum-well width larger than 190 Å, which is due to the onset of the three-subband transport.

Figure 8 shows the results at 300 K and the total mobility is almost determined by the polar optical-phonon scattering. As compared with the case for the GaAs quantum well, the variations of mobility with the change of quantum-well width are more conspicuous. This is considered to be due to the larger energy separation of subband levels of E_0 and E_1 that resulted from the larger conduction-band discontinuity ΔE_c. Although the agreement between the calculated and measured results is fairly good, all the calculated results showed higher mobilities than the measured ones by about 30% when the effective mass of $0.0604m_0$ was used. So far we did not take the nonparabolicity effect on electron mass into consideration, but this effect may become important in the pseudomorphic quantum-well system. Contrary to our assumption of electron mass (that it becomes lighter with increasing InAs mole fraction), the reported electron

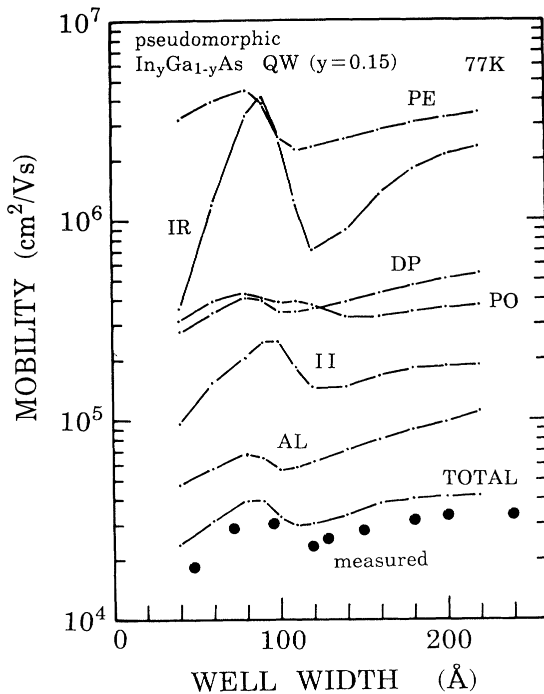

FIG. 7. Calculated and measured electron mobility in $Al_xGa_{1-x}As$/$In_yGa_{1-y}As$/$Al_xGa_{1-x}As$ heterostructures ($x=0.27$, $y=0.15$) at 77 K as a function of $In_yGa_{1-y}As$ quantum-well width.

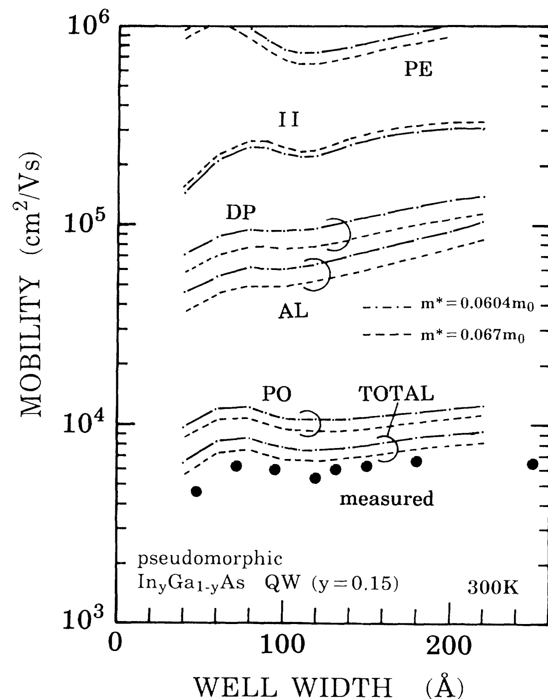

FIG. 8. Calculated and measured electron mobility in $Al_xGa_{1-x}As$/$In_yGa_{1-y}As$/$Al_xGa_{1-x}As$ heterostructures ($x=0.27$, $y=0.15$) at 300 K as a function of $In_yGa_{1-y}As$ quantum-well width.

mass measured by a cyclotron resonance method shows no InAs mole fraction dependence.[24] Such constancy of electron mass can be also obtained by using the first-order $\mathbf{k}\cdot\mathbf{p}$ theory.[25] Therefore, in order to clarify the effect of electron mass, we have recalculated the electron mobilities by setting the effective electron mass in an $In_yGa_{1-y}As$ quantum well to that of bulk GaAs ($0.067m_0$). The results are shown in Fig. 8 by dashed lines and it can be seen that the agreement between the calculated and measured mobilities has been very much improved. From this result, the inclusion of nonparabolicity effects into the mobility calculations seems to be necessary and important, especially for pseudomorphic heterostructures. Although the two-subband transport model is considered to be applicable for low-temperature regions, this result shows that, in some cases, it can be applied to wider temperature regions when the energy separation of subbands in the quantum well is relatively large.

IV. SUMMARY

In summary, electron mobilities in modulation-doped $Al_xGa_{1-x}As/GaAs/Al_xGa_{1-x}As$ and pseudomorphic $Al_xGa_{1-x}As/In_yGa_{1-y}As/Al_xGa_{1-x}As$ quantum-well heterostructures with high electron concentrations were analyzed using two-subband transport model. The experimental variations of mobilities with the change of the quantum-well width in these heterostructures were well explained by theoretical calculations based on this model. It has been found that the highest mobility at 77 K is obtained for the quantum-well widths from 80 to 100 Å, at which almost all the electrons populate in the ground subband and their Fermi energy has a maximum value. The two-subband model has been shown to be applicable also to the mobility calculations at 300 K for some cases when the separation of subband energies is relatively large.

ACKNOWLEDGMENTS

The authors would like to express their sincere thanks to Dr. N. Sato for valuable discussions and to Dr. T. Takemoto and T. Onuma for their continuous encouragement throughout this work.

[1] W. Walukiewicz, H. E. Ruda, J. Lagowsky, and H. C. Gatos, Phys. Rev. B **29**, 4818 (1984).
[2] K. Hirakawa and H. Sakaki, Phys. Rev. B **33**, 8291 (1986).
[3] S. Mori and T. Ando, Phys. Rev. B **19**, 6433 (1979).
[4] E. D. Sigga and P. C. Kwock, Phys. Rev. B **2**, 1024 (1970).
[5] G. Fishman and D. Calecki, Phys. Rev. B **29**, 5778 (1984).
[6] S. Mori and T. Ando, J. Phys. Soc. Jpn. **48**, 865 (1980).
[7] B. Vinter, Appl. Phys. Lett. **45**, 581 (1984).
[8] B. R. Nag, *Electron Transport in Compound Semiconductors* (Springer-Verlag, Berlin, 1980).
[9] P. J. Price, J. Vac. Sci. Technol. **19**, 599 (1981).
[10] T. Ando, A. Fowler, and F. Stern, Rev. Mod. Phys. **54**, 437 (1982).
[11] P. F. Maldague, Surf. Sci. **113**, 199 (1978).
[12] J. W. Harrison and J. R. Hauser, Phys. Rev. B **13**, 5347 (1976).
[13] M. A. Littlejohn, J. R. Hauser, and T. H. Glisson, Solid-State Electron. **21**, 107 (1978).
[14] R. E. Prange and T. W. Nee, Phys. Rev. **168**, 779 (1968).
[15] S. Mori and T. Ando, J. Phys. Soc. Jpn **48**, 865 (1980).
[16] K. Inoue, H. Sakaki, and T. Hotta, J. Appl. Phys. **58**, 4277 (1985).
[17] F. Stern and S. Das Sarma, Phys. Rev. B **30**, 840 (1984).
[18] R. Chwang, B. J. Smith, and C. R. Crowell, Solid-State Electron. **17**, 1217 (1974).
[19] R. C. Miller, D. A. Kleinmann, and A. C. Gossard, Phys. Rev. B **29**, 7085 (1984).
[20] A. Gold, Phys. Rev. B **35**, 723 (1987).
[21] H. Sakaki, T. Noda, K. Hirakawa, M. Tanaka, and T. Matsusue, Appl. Phys. Lett. **51**, 1934 (1987).
[22] K. Inoue, H. Sakaki, J. Yoshino, and Y. Yoshioka, Appl. Phys. Lett. **46**, 973 (1985).
[23] G. Ji, D. Haung, U. K. Reddy, T. S. Henderson, R. Houdre, and H. Morkoc, J. Appl. Phys. **62**, 3366 (1987).
[24] C. T. Liu, S. Y. Lin, D. C. Tsui, H. Lee, and D. Ackley, Appl. Phys. Lett. **53**, 2510 (1988).
[25] I. Suemune, IEEE J. Quantum Electron. **QE-27**, 1149 (1991).